Transition from minority to majority spin transport in iron-manganese nitride $Fe_{4-x}Mn_xN$ films with increasing x

Akihito Anzai,[1] Toshiki Gushi,[1,2] Taro Komori,[1] Syuta Honda,[3,4] Shinji Isogami,[5] and Takashi Suemasu[1]

[1]*Institute of Applied Physics, Graduate School of Pure and Applied Sciences, University of Tsukuba, Tsukuba, Ibaraki 305-8573, Japan*
[2]*University Grenoble Alpes, CEA, CNRS, Grenoble 38000, France*
[3]*Department of Pure and Applied Physics, Faculty of Engineering Science, Kansai University, Suita 564-8680, Japan*
[4]*Center for Spintronics Research Network, Osaka University, Toyonaka 560-8531, Japan*
[5]*Research Center for Magnetic and Spintronic Materials, National Institute for Materials Science (NIMS), Tsukuba 305-0047, Japan*

(Received 11 August 2018; accepted 10 September 2018; published online 28 September 2018)

Herein, 30 nm-thick $Fe_{4-x}Mn_xN$ ($x = 0$, 1, 2, 3, and 4) epitaxial films were grown on MgO(001) substrates by molecular beam epitaxy, and the anisotropic magnetoresistance (AMR) properties were measured at temperatures (T) between 10 and 300 K. A negative AMR effect was observed in the Fe_4N and $FeMn_3N$ films at $T \leq 300$ K and in the Mn_4N film at $T \leq 100$ K. In contrast, a positive AMR effect was observed in the Fe_3MnN and Fe_2Mn_2N films at $T \leq 300$ K. Using the relationship between the AMR ratio, the spin polarization of the density of states at the Fermi level, and the spin polarization of the electrical conductivity (P_σ), we derived the sign of P_σ to be negative in Fe_4N, Fe_3MnN, and Fe_2Mn_2N and to be positive in $FeMn_3N$ and Mn_4N. These results show that the minority spin transport is dominant in $Fe_{4-x}Mn_xN$ for $x = 0$, 1, and 2 at lower temperatures, whereas the majority spin transport is dominant with increasing x in $Fe_{4-x}Mn_xN$ for $x = 3$ and 4. *Published by AIP Publishing.* https://doi.org/10.1063/1.5051721

I. INTRODUCTION

Anti-perovskite 3*d* nitrides and their mixed crystals have been investigated as spintronics materials both with theory and experiment.[1–10] One of these nitrides, Mn_4N, satisfies both of the requirements of a perpendicular magnetic anisotropy (PMA) and a small saturation magnetization (M_S). Specifically, a PMA has been reported for Mn_4N films grown on substrates composed of glass,[11] Si(001),[12] MgO(001),[13–17] and $SrTiO_3$(001).[13,18] Furthermore, the Mn_4N is a ferrimagnetic metal with $M_S = 182$ emu/cm^3 at 77 K and a high Curie temperature of 745 K.[1] Recently, we have achieved spin-transfer-torque-driven domain wall velocities greater than 230 m/s with current densities as small as 7×10^{11} A/m^2 in 1–2 μm-wide Mn_4N strips.[19] These velocities surpass those found in FeNi (~100 m/s).[20] Such a fast domain wall propagation in Mn_4N is ascribed to the low M_S value and the presence of a PMA, originating from the specific chemical bonding between Mn and N atoms in the anti-perovskite unit cell. The lattice structure of Mn_4N is shown in Fig. 1. The Mn atoms occupy the corner (I) and face-centered (II) sites and the N atom occupies the body-centered site. The II sites are further divided into IIA and IIB sites in the presence of magnetization (M) (arrow in Fig. 1).

Substitution of other 3*d* transition metal atoms for the Mn atoms in Mn_4N is an effective means to change the magnetic properties. For example, in $Mn_{4-y}Co_yN$, there is a tendency for the anisotropy field to increase as the Co content (i.e., y value) increases, whereas the M_S and uniaxial magnetic anisotropy energy decrease.[18] However, the formation of $Mn_{4-y}Co_yN$ is difficult to achieve because of the phase separation, and thus, the y value of $Mn_{4-y}Co_yN$ is limited to ≤0.2. Another example is $Fe_{4-x}Mn_xN$.[21–24] Although the magnetic properties of $Fe_{4-x}Mn_xN$ have been theoretically predicted,[21–23] its formation has been limited to powders with a small Mn content ($x \leq 0.75$). Very recently, we have achieved the epitaxial growth of $Fe_{4-x}Mn_xN$ ($x = 0$, 1, 2, 3, and 4) films by molecular beam epitaxy (MBE) and characterized their M_S values at room temperature (RT).[25] A PMA was observed in $Fe_{4-x}Mn_xN$ films at $x = 3$ and 4 at RT, though no PMA existed at $x \leq 2$. However, the spin-polarization (P_D) of the density of states (D) at the Fermi level (E_F), $P_D = [D_\uparrow(E_F) - D_\downarrow(E_F)]/[D_\uparrow(E_F) + D_\downarrow(E_F)]$, and the spin polarization of the electrical conductivity (σ), $P_\sigma = (\sigma_\uparrow - \sigma_\downarrow)/(\sigma_\uparrow + \sigma_\downarrow)$, have yet to be investigated. Regarding ferromagnetic Fe_4N, Kokado *et al.* have calculated its P_D and P_σ values to be −0.6 and −1.0, respectively.[26] However, it has been considered difficult to experimentally obtain the sign of P_σ, though the sign is very important for devices wherein electrical conductivity plays a major role, such as giant magnetoresistance devices. Recently, several studies on magnetotransport properties in ferromagnetic materials such as the anisotropic magnetoresistance (AMR) effect have been conducted theoretically[27–29] and experimentally.[30–40] Kokado *et al.* have derived a general expression between the AMR ratio γ_{AMR}, P_D, and P_σ such that

$$\gamma_{AMR} \propto -\left(\frac{\lambda}{H_{ex}}\right)^2 P_D P_\sigma, \quad (1)$$

which was derived from the two-current model[27] comprising a spin-polarized conduction state and localized *d* states

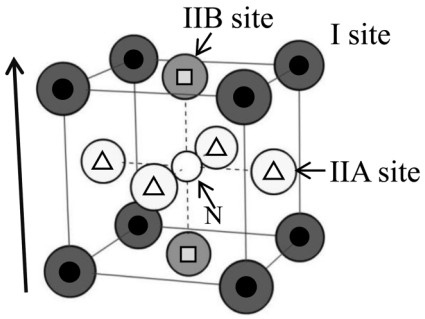

FIG. 1. Crystal structure of anti-perovskite-type 3*d* transition metal nitride. The II sites can be divided into IIA and IIB sites depending on the magnetization direction (arrow).

within the spin-orbit interaction. Here, λ is the spin-orbit coupling constant and H_{ex} is the exchange field. This enables the derivation of the sign of P_σ from those of P_D and γ_{AMR}. Using this expression, the fact that the minority spins dominate the electrical conductivity in Fe_4N has been confirmed by the negative γ_{AMR}.[30–35] This was the motivation to achieve the inverse current-perpendicular-to-plane giant magnetoresistance effect in Fe_4N/Ag/Fe structures at RT.[41] In the same manner, we have confirmed a negative sign for P_σ in Co_3FeN,[34] Fe_3NiN, and $FeNi_3N$ epitaxial films.[42] In this study, we measured the γ_{AMR} of $Fe_{4-x}Mn_xN$ ($x = 0$, 1, 2, 3, and 4) films grown on MgO(001) single-crystal substrates and investigated their sign from the magnetotransport properties.

II. METHODS

A. Formation and characterization of $Fe_{4-x}Mn_xN$ films

The 30 nm-thick $Fe_{4-x}Mn_xN$ ($x = 0$, 1, 2, 3, and 4) epitaxial thin films were grown on MgO(001) single-crystal substrates by MBE using solid sources of Mn and Fe and radio-frequency nitrogen plasma. The substrate temperature (T_{sub}) was varied from 350 to 550 °C to determine the optimum temperature for each composition. The fabrication has been previously detailed in Ref. 25. Nitrogen ions were eliminated by applying bias voltages to the plasma generator, while the Mn/Fe ratio was controlled by the deposition rate (nm/min) based on the crucible temperature of the Knudsen cells. The crystalline quality of the samples was evaluated by reflection high-energy electron diffraction (RHEED) and by out-of-plane and in-plane X-ray diffraction (XRD; SmartLab, Rigaku Inc.) measurements with Cu-$K\alpha$ radiation. In the XRD measurements, a Ge(220) single crystal was used to monochromatize the X-ray beam. The magnetization versus magnetic field (M–H) curves were measured by a vibrating sample magnetometer (VSM) at RT. To calculate the sample thickness excluding the surface oxidation layer, we used an X-ray reflectivity measurement. The AMR measurements were performed for $2 \times 6\ mm^2$ rectangular samples using a physical property measurement system (Quantum Design) equipped with a motorized sample rotator in the temperature T range of 10–300 K. The measurements were performed using the direct-current four-probe method with an external magnetic field (H) of 40 kOe and a current I of 0.1 mA along the [100] axis of the epitaxial layer. The in-plane relative angle ϕ between H and I was varied from 0° to 360°, and the ϕ dependence of the resistivity $\rho(\phi)$ was measured. The direction of M corresponded to that of H because the magnitude of H was sufficiently large to saturate the sample magnetization.

B. Computational details

We calculated the density of states, the M_S values, and the total energy using the Vienna *ab initio* simulation package[43] (VASP) via projector augmented wave psedopotenials,[44] spin-polarized Perdew-Burke-Ernzerhof generalized gradient approximations,[45] and Bader charge analysis.[46] The total energy minimization was obtained via an optimization of the lattice parameters and a relaxation of the atomic positions in a conjugate gradient routine. The convergence in the total energy was better than 10^{-6} eV/f.u. using the energy cutoff of 400 eV. The k-point sampling of $27 \times 27 \times 27$ was used for the calculation of the charge density with VASP. By performing the calculation for structural relaxation, formation energy, lattice parameters (a and c), and spin magnetic moment, the values of M_S, D, and P_D were calculated. We considered two model types for $Fe_{4-x}Mn_xN$ ($x = 1$, 2, and 3), notated as types A and B, for both Fe_3MnN and $FeMn_3N$. In a unit cell of type A Fe_3MnN (type A $FeMn_3N$), Fe (Mn) atoms are positioned at the IIA and IIB sites, while Fe (Mn) atoms occupy the I and IIA sites in type B Fe_3MnN (type B $FeMn_3N$). Two types of unit cells of Fe_2Mn_2N also exist, whereby Fe_2Mn_2N (corner: Fe) exhibits Fe atoms positioned at the I and IIB sites, while Mn atoms occupy the IIA sites. In a unit cell of Fe_2Mn_2N (corner: Mn), however, Mn atoms occupy the I and IIB sites, and Fe atoms occupy the IIA sites. The calculated M_S values and formation energies of the eight types of lattices are summarized in Table I.

III. RESULTS AND DISCUSSION

A. Structural investigation

Figure 2 shows the out-of-plane XRD and RHEED patterns of 30 nm-thick $Fe_{4-x}Mn_xN$ ($x = 0$, 1, 2, 3, and 4) films grown at $T_{sub} = 450$ °C for $x = 0$ and 2, and at $T_{sub} = 550$ °C for $x = 1$, 3, and 4. These T_{sub} values were chosen to minimize the full width at half maximum of the $Fe_{4-x}Mn_xN$ 002 diffraction peaks for each sample by ω-scan X-ray rocking

TABLE I. Calculated M_S values and formation energies for $Fe_{4-x}Mn_xN$ compounds with $x = 0$–4.

Compound	M_S (emu/cm^3)	Formation energy (eV/cell)
Fe_4N	1698.03	−5.22397
Fe_3MnN (type A)	1767.90	−4.98372
Fe_3MnN (type B)	771.60	−5.22894
Fe_2Mn_2N (corner: Fe)	545.33	−5.17169
Fe_2Mn_2N (corner: Mn)	665.38	−5.37556
$FeMn_3N$ (type A)	476.12	−5.28342
$FeMn_3N$ (type B)	410.98	−5.49424
Mn_4N	211.91	−5.57043

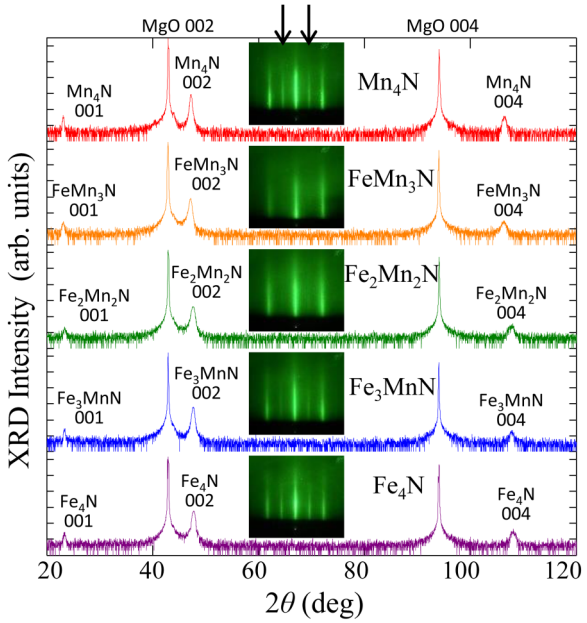

FIG. 2. Out-of-plane XRD and RHEED patterns of $Fe_{4-x}Mn_xN$ along the MgO[100]. The arrows indicate the position of superlattice diffraction lines.

curve measurements. Streaky RHEED patterns and *c*-axis-oriented XRD diffraction peaks corresponding to the nitride phase were observed for all samples. These results demonstrate that single-phase nitrides were epitaxially grown on the MgO(001) substrates. In the RHEED patterns shown in Fig. 3, superlattice diffractions from N atoms at the body-centered site (arrows in Fig. 3) were clearly observed in the Mn_4N, Fe_3MnN, and Fe_4N films, indicating that the N atoms were long-range ordered, whereas those lines were blurred in the $FeMn_3N$ and Fe_2Mn_2N films. In the XRD patterns, such superlattice peaks appeared in all of the samples, demonstrating the presence of N atoms at the correct positions in these films. The *c*-axis-oriented diffraction peaks of $Fe_{4-x}Mn_xN$ shifted to lower angles with the Mn content, signifying that the lattice constant *c* increased. This shift is the result of the Mn_4N possessing a larger lattice constant than that of Fe_4N. As an index for N atoms to be correctly located at the body-centered sites, we employed the degree of order of N (S). S is defined as the correctness of the N atom location, namely, the occupation probability is $(1+3S)/4$ for the assigned body-centered site and is determined as[33]

$$S = \sqrt{\frac{I_{100}^{\mathrm{obs}}/I_{200}^{\mathrm{obs}}}{I_{100}^{\mathrm{cal}}/I_{200}^{\mathrm{cal}}}}, \tag{2}$$

$$I_{hkl}^{\mathrm{cal}} = LP \cdot \Psi \cdot F_{hkl}^2 \cdot \exp\left(-2B\frac{\sin^2\theta}{\lambda^2}\right), \tag{3}$$

where I_{hkl}^{obs} and I_{hkl}^{cal} are the integrated XRD intensities of the *hkl* reflection obtained by experiment and calculation, respectively; LP is the Lorentz-polarization factor for a single crystal; Ψ is the powder ring distribution factor;[47] and the exponential term is the Debye-Waller factor, where B is the temperature factor, F_{hkl} is the structure factor of the $Mn_{4-x}Fe_xN$ unit cell for *hkl* diffraction, and λ is the wavelength of x-ray used ($\lambda = 0.15418$ nm). For an in-plane geometry, Ψ was obtained using Eq. (5) in Ref. 47, where the equipment parameter s_2 was fixed as 3.3° by using the angular divergence of the detector window. Herein, LP was calculated by

$$LP = \frac{1+\cos^2(2\theta)\cos^2(2\theta_{\mathrm{M}})}{\sin 2\theta\{1+(\cos^2\theta_{\mathrm{M}})\}}, \tag{4}$$

where θ_{M} is the Bragg angle of the monochromator. Considering its crystalline structure, F_{hkl} of Mn_4N is

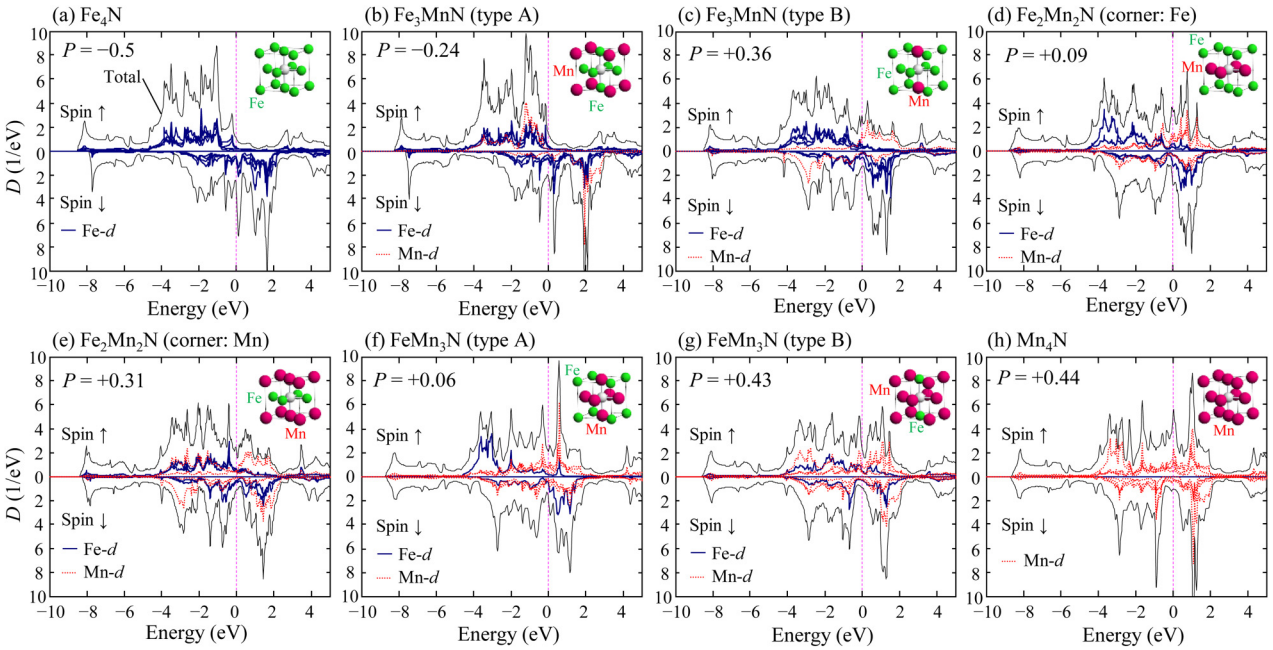

FIG. 3. Calculated spin-resolved partial D and total D of $Fe_{4-x}Mn_xN$ ($x = 0$, 1, 2, 3, and 4). Calculated values of P_{D} at E_{F} are presented.

defined as

$$F_{hkl} = f_{Mn}\{1 + (-1)^{h+k} + (-1)^{k+l} + (-1)^{l+h}\} + f_N(-1)^{h+k+l}. \quad (5)$$

Here, f_{Mn} and f_N are the atomic scattering factors of Mn and N atoms, respectively. In $Mn_{4-x}Fe_xN$, we estimated that the Mn and Fe atoms were randomly distributed at the I and II sites, and thus, F_{hkl} of $Mn_{4-x}Fe_xN$ was calculated using

$$F_{hkl} = \left\{\frac{x \cdot f_{Fe} + (4-x) \cdot f_{Mn}}{4}\right\}\{1 + (-1)^{h+k} + (-1)^{k+l} + (-1)^{l+h}\} + f_N(-1)^{h+k+l}. \quad (6)$$

Here, f_{Fe} is the atomic scattering factor of Fe atom. The parameter B was calculated by rearranging Eq. (3) and obtaining $-2B = \ln[I_{obs}/\{{F_{hkl}}^2 \cdot LP \cdot \Psi\}]/(\sin\theta/\lambda)^2$, where I_{obs} is the integrated intensity of the experimentally obtained diffraction peak. Herein, we calculated B by logarithmically plotting the I_{obs} of the 200, 220, and 400 diffractions as a function of their angles and fitting the curves using the least squares method. S values together with the ratio of the perpendicular lattice constant c to the in-plane lattice constant a (c/a) were summarized in Table II. The values of c/a were found to be 1.005 in Fe_4N, 0.985 in Fe_2Mn_2N, 0.986 in $FeMn_3N$, and 0.991 in Mn_4N. This means the presence of an in-plane tensile strain at RT, and thus, the tetragonal distortion exists. We should notice that the S value was as small as approximately 0.5 in the Fe_2Mn_2N and $FeMn_3N$ films. We attribute such small S values to crystal imperfections in these films. This is apparent from the blurred RHEED patterns of these films as shown in Fig. 2.

B. Calculation results

Here, we present the calculation results for D and M_S in the $Fe_{4-x}Mn_xN$ according to the *ab initio* calculations. Several metastable states possessing different M_S values were calculated for the three $Fe_{4-x}Mn_xN$ compositions with $x = 1$, 2, and 3. In the $Fe_{4-x}Mn_xN$ with $x = 1$, the energy of the calculated lowest energy state of the Fe_3MnN (type B) was lower than that of the Fe_3MnN (type A) (Table I). Hence, the lowest energy state for the Fe_3MnN (type A) is a metastable state within the same compositional Fe_3MnN, and therefore, this calculated result recommends the Fe_3MnN (type B) structure. Similarly, in the $Fe_{4-x}Mn_xN$ with $x = 2$ and 3, the structures possessing type B and corner Mn are the most stable structures within the same $Fe_{4-x}Mn_xN$ composition.

TABLE II. Values of c/a obtained from XRD analysis and degree of order (S) of N site for $Fe_{4-x}Mn_xN$ compounds with $x = 0$–4.

Compound	c/a	S
Fe_4N	1.005	0.82
Fe_3MnN	1.001	0.68
Fe_2Mn_2N	0.985	0.52
$FeMn_3N$	0.986	0.55
Mn_4N	0.991	0.70

Figure 3 shows the calculated spin-resolved partial D and total D values for the lowest energy state of each $Fe_{4-x}Mn_xN$ ($x = 0$, 1, 2, 3, and 4) structure. The calculated values of P_D at E_F ($E = 0$) are also represented. With the increase of Mn content x, the exchange splitting decreases and the E_F shifts deep into the ↑-spin bands. The P_D values for the Fe_4N [Fig. 3(a)] and Mn_4N [Fig. 3(h)] are a negative value of −0.5 and a positive value of +0.44, respectively. The total D value of the Fe_3MnN (type A) [Fig. 3(b)] is similar to that of the Fe_4N [Fig. 3(a)], and the P_D value is negative. In this structure, the d states at Fe are representative at the E_F. Meanwhile, the total D values for the other $Fe_{4-x}Mn_xN$ ($x = 1$, 2, and 3) structures [Figs. 3(c)–3(g)] are similar to those calculated for the Mn_4N [Fig. 3(h)], and all P_D values are positive. The values of P_D for Fe_2Mn_2N (corner Mn) and $FeMn_3N$ (type B), which are the most stable structures, respectively, for $x = 2$ and 3 for $Fe_{4-x}Mn_xN$, are as large as +0.36 and +0.43, respectively. However, the absolute values of P_D for the Fe_2Mn_2N (corner Fe) and the $FeMn_3N$ (type A), which are not the most stable structures within the same compositional $Fe_{4-x}Mn_xN$, are as small as 0.09 and 0.06, respectively. In these five structures, the d states at Mn are representative at the E_F. It should also be noted in Fig. 3 that the E_F is located close to the energy where the total D reaches a maximal value in Fe_4N and Mn_4N. This result suggests that the P_D is considered sensitive to T in these materials.

Figure 4 shows the calculated M_S values associated with the structure for the density of states D shown in Fig. 3, alongside the measured values of M_S (closed squares in Fig. 4). With the exception of the Fe_3MnN (type A), the calculated M_S of $Fe_{4-x}Mn_xN$ decreases with increasing x value, which is consistent with the experimentally measured values. The M_S value of Fe_3MnN (type A) (1767.90 emu/cm^3) is larger than that of Fe_4N (1698.03 emu/cm^3), but the energy of the state of Fe_3MnN (type A) is larger than that of the lowest energy state of Fe_3MnN (type B). Therefore, considering both the calculated energy for each Fe_3MnN type and the comparison between the calculated and measurement magnetization, the $Fe_{4-x}Mn_xN$ (type B and corner: Mn) structures are recommended. The deviation of the measured M_S values

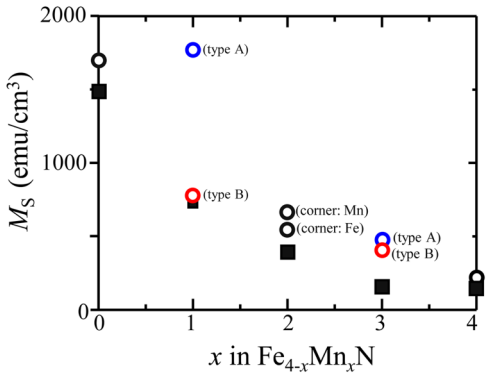

FIG. 4. Calculated (hollow circles) and experimentally obtained (solid squares) saturation magnetization M_S values of $Fe_{4-x}Mn_xN$ films as a function of x at room temperature.

from those calculated was distinct in Fe_4N, Fe_2Mn_2N, and $FeMn_3N$. We attribute this deviation to crystal imperfections in these films with reduced S values as shown in Table II.

C. Temperature dependence of the AMR effect

Figure 5 shows the AMR curves of $Fe_{4-x}Mn_xN$ epitaxial films with a current I set along the [100] axis of the epitaxial layer, given by the angular dependence of the resistivity change normalized by $\rho(90°)$ such that $[\rho(\phi)-\rho(90°)]/\rho(90°)$. The AMR ratio γ_{AMR} is obtained at $\phi = 0°$ and 180°. It is apparent that these curves significantly depend on both T and ϕ. As will be discussed later, these curves can be fitted using the two cosine functions of $\cos(2\phi)$ and $\cos(4\phi)$. Examining the AMR curves in Fig. 5 is apparent that the $\cos(4\phi)$ component is dominant in Mn_4N. A similar result has been previously reported in Ref. 17. In-depth discussions about the origin of the ϕ dependence of γ_{AMR} are provided in Refs. 28 and 29. Briefly, it originates from the dependence of the electron occupation of $3d$ orbitals on the direction of magnetic moment with respect to the crystal axes. This is because the AMR effect is attributed to the spin-orbit interaction, which causes spin mixing in the scattering process of conduction electrons into $3d$ orbitals.[48,49] The $\cos(2\phi)$ term arises from the twofold symmetry of $3d$ orbitals due to the spin-orbit interactions.[28] On the other hand, the $\cos(4\phi)$ term is attributed to the fourfold symmetry of $3d$ orbitals caused by the tetragonal distortion.[29] The presence of tetragonal distortion was confirmed in Fe_4N by the transverse AMR effect,[40] where the magnetization vector was rotated in the orthogonal plane to the current direction.

Figure 6 shows the T dependences of γ_{AMR}. The sign of γ_{AMR} is positive for Fe_3MnN and Fe_2Mn_2N at $T \leq 300$ K but is negative for Fe_4N and $FeMn_3N$ at $T \leq 300$ K. Regarding Mn_4N, γ_{AMR} is positive at 300 K and negative at $T \leq 100$ K. The signs of all of the calculated γ_{AMR} values are summarized in Table III. We next deduced the sign of P_σ using Eq. (1). Because 0 K is assumed in the calculation, our discussion on the sign of P_σ is limited to low temperatures. From Eq. (1), when P_D and γ_{AMR} have the same sign, the sign of P_σ is negative, and when P_D and γ_{AMR} exhibit opposite signs, the sign of P_σ is positive. These results can be seen in Table III, where P_σ is negative for Fe_4N, Fe_3MnN, and Fe_2Mn_2N, and is positive for $FeMn_3N$ and Mn_4N. We therefore can posit that minority spin conduction is dominant in Fe_4N, Fe_3MnN, and Fe_2Mn_2N, whereas majority spin conduction is dominant in $FeMn_3N$ and Mn_4N. These results demonstrate the gradual change from a negative P_σ in Fe_4N (i.e., $x = 0$) to a positive P_σ in Mn_4N (i.e., $x = 4$) with increasing x in $Fe_{4-x}Mn_xN$ (Table III).

Figure 7 shows the Fourier coefficients of the AMR curves obtained for $Fe_{4-x}Mn_xN$ using the least squares fitting method with

$$[\rho(\phi)-\rho(90^\circ)]/\rho(90^\circ) = C_0 + C_2\cos(2\phi) + C_4\cos(4\phi), \quad (7)$$

where C_2 and C_4 are the Fourier coefficients of the $\cos(2\phi)$ and $\cos(4\phi)$ components, respectively, and C_0 ($=C_2 - C_4$) is

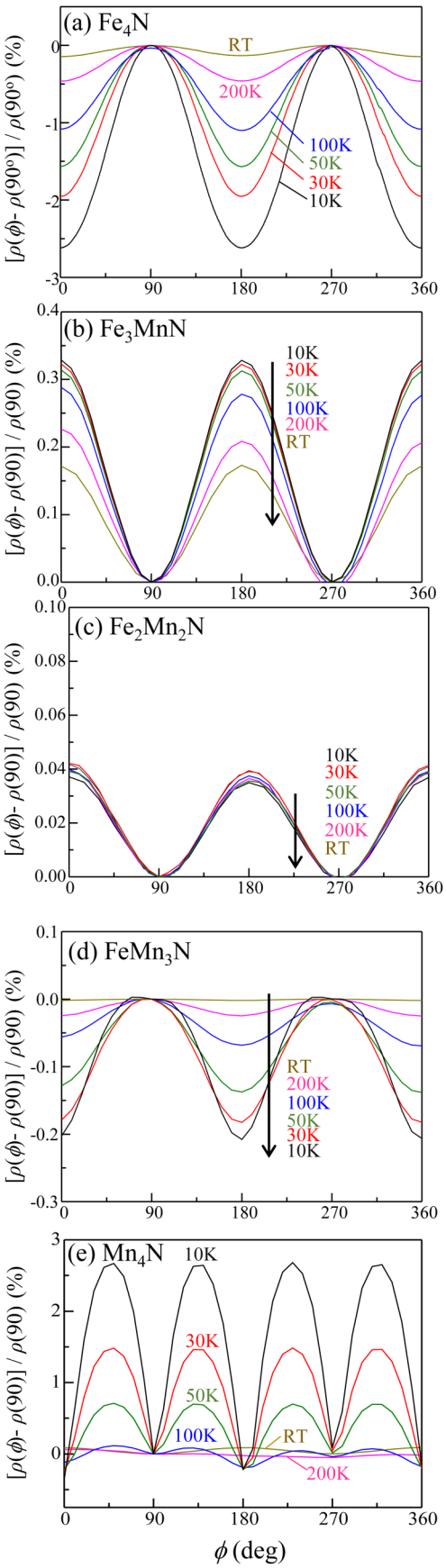

FIG. 5. Anisotropic magnetoresistance $[\rho(\phi)-\rho(90°)]/\rho(90°)$ curves of (a) Fe_4N, (b) Fe_3MnN, (c) Fe_2Mn_2N, (d) $FeMn_3N$, and (e) Mn_4N films measured in the 300–10 K temperature range. The sensing current was set along the [100] axis of the grown films.

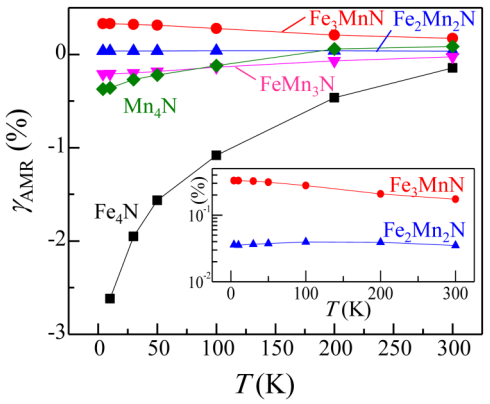

FIG. 6. γ_{AMR} values of the $Fe_{4-x}Mn_xN$ films as a function of temperature.

a constant. The derivation of Eq. (7) is presented, for example, in Ref. 42. Although this equation was originally derived from the phenomenological expressions,[50] Kokado and Tsunoda derived Eq. (7) from the framework of transport theory and gave the physical explanations to it.[29] It was reported that C_4 appears under the crystal field of tetragonal symmetry at low temperatures, whereas it vanishes under the crystal field of cubic symmetry. The tetragonal distortion is assumed to originate from the anisotropic thermal compression of the lattice caused by the adhesion between the grown layer and the MgO substrate. Furthermore, γ_{AMR} directly relates to C_2 such that $\gamma_{AMR} = 2C_2$. Thereby, we are able to understand the T dependence of γ_{AMR} and the degree of the tetragonal distortion in $Fe_{4-x}Mn_xN$ films by obtaining the T dependence of C_2 and C_4.

First, we discuss the C_2 term. As shown in Fig. 7, the decrease in $|C_2|$ with increasing T was observed for all samples except Fe_2Mn_2N, leading to the reduction in $|\gamma_{AMR}|$ at higher T as shown in Fig. 6. We ascribe the decrease in $|C_2|$ thereby $|\gamma_{AMR}|$ with an increase of T to the decrease in $|P_D|$ and $|P_\sigma|$ in Eq. (1). In Fig. 7, there is a distinct difference in C_2 values between the Fe_4N and Mn_4N structures. Specifically, in Fe_4N,[33,34] the C_2 is negative over the entire T range and the $|C_2|$ begins to significantly increase at $T < 100$ K. We speculate that such a drastic change in $|C_2|$ in Fe_4N is attributed to the fact that the total D reaches a maximal value at around E_F as shown in Fig. 3(a), and thus the P_D is sensitive to T. Conversely, in Mn_4N, the C_2 is positive at 300 K but changes to a negative value at lower T. Similar result was obtained previously.[17] The C_2 is negative in $FeMn_3N$, and the $|C_2|$ shows a gradual increase with decreasing T. In Fe_2Mn_2N with a small S value, however, the C_2 value does not significantly change across the whole T range. Kabara *et al.* systematically investigated the influence of S on the C_2 and C_4 terms in Fe_4N and found that with decreasing S the enhancement of C_2 at low temperatures gradually decreased, and C_4 vanished.[33] Therefore, it can be stated that the crystal field effect can be deteriorated by the reduction of S thereby crystal imperfections. Here, we discuss the sign of C_2 in more detail mainly on Fe_4N and Mn_4N using Fig. 8. The 3d orbitals of Fe_4N are split into the two states d_ε and d_γ by a cubic crystal field effect. These states are then further split into finer states such as $d_\varepsilon \rightarrow d_{\delta\varepsilon}$ (d_{xy}, d_{yz}, d_{zx}) and $d_\gamma \rightarrow d_{3z^2-r^2}, d_{x^2-y^2}$ by a tetragonal distortion.[29] Here, it is assumed that the sample and the magnetic moment M are on the x-y plane and the current I flows in the x-direction. ϕ is the relative angle between I and M. According to Ref. 29, when the dominant s–d scattering process is $s_{\uparrow(\downarrow)} \rightarrow d_{\downarrow(\uparrow)}$, which signifies that the ↑(↓)-spin conduction electrons are scattered into ↓(↑)-spin d bands, the C_2 is described as

$$C_2^{s_{\uparrow(\downarrow)} \rightarrow d_{\downarrow(\uparrow)}} \propto \left(\frac{\lambda}{H_{ex} - \Delta}\right)^2 D_{\xi,\downarrow(\uparrow)}, \tag{8}$$

where Δ and $D_{\xi,\varsigma}$ are the energy difference between the d_ε and d_γ states, and the partial D of the d_ξ orbital in the d_ε states with ς-spin at E_F, respectively. In this case, C_2 is always positive. Conversely, in the case where the $s_{\uparrow(\downarrow)} \rightarrow d_{\uparrow(\downarrow)}$ scattering process is dominant, the dominant term in C_2 is proportional to the difference in the partial D at E_F between the d_ε and d_γ states, and is described as

$$C_2^{s_{\uparrow(\downarrow)} \rightarrow d_{\uparrow(\downarrow)}} \propto \left(\frac{\lambda}{\Delta}\right)^2 (D_{\gamma,\uparrow(\downarrow)} - D_{\delta\varepsilon,\uparrow(\downarrow)}), \tag{9}$$

where $D_{\gamma(\delta\varepsilon),\varsigma}$ is the partial D of the $d_{\gamma(\delta\varepsilon)}$ orbital with a ς-spin at E_F. Because C_2 is negative for Fe_4N at $T \leq 300$ K and the $|C_2|$ value increases with the decrease of T, we assume from Eq. (4) that the partial D of the d_γ states in that structure is smaller than that of the d_ε states at E_F, and the $|D_{\gamma,\uparrow(\downarrow)} - D_{\delta\varepsilon,\uparrow(\downarrow)}|$ increases with decreasing T. As the P_σ is negative in Fe_4N, as shown in Table III, the ↓-spin electrons dominate the electrical conduction and are scattered into ↓-spin d bands. In the case of ferrimagnetic Mn_4N, however, additional theoretical considerations are required.[17] This is because the magnetic moment of Mn atoms at I sites is antiparallel to that at II sites.[1] Mn atoms thus can be grouped into two from the viewpoint of magnetic moment. They are named sublattices A and B, corresponding to the lattices composed of Mn atoms at I sites and II sites, respectively. Thus, Eqs. (8) and (9) are, respectively, modified to[17]

$$C_2^{s_{\uparrow(\downarrow)} \rightarrow d_{\downarrow(\uparrow)}} \propto \left(\frac{\lambda}{H_A - \Delta}\right)^2 D_{A,\xi,\downarrow(\uparrow)} + \left(\frac{\lambda}{-H_B - \Delta}\right)^2 D_{B,\xi,\downarrow(\uparrow)}, \tag{10}$$

$$C_2^{s_{\uparrow(\downarrow)} \rightarrow d_{\uparrow(\downarrow)}} \propto \left(\frac{\lambda}{\Delta}\right)^2 \{(D_{A,\gamma,\uparrow(\downarrow)} + D_{B,\gamma,\uparrow(\downarrow)}) - (D_{A,\delta\varepsilon,\uparrow(\downarrow)} + D_{B,\delta\varepsilon,\uparrow(\downarrow)})\}, \tag{11}$$

TABLE III. Signs of the γ_{AMR}, P_D at E_F, and P_σ parameters in $Fe_{4-x}Mn_xN$.

Compound	γ_{AMR}	P_D at E_F	P_σ
Fe_4N	−	−	−
Fe_3MnN (type B)	+	+	−
Fe_2Mn_2N (corner: Mn)	+	+	−
$FeMn_3N$ (type B)	−	+	+
Mn_4N	−	+	+

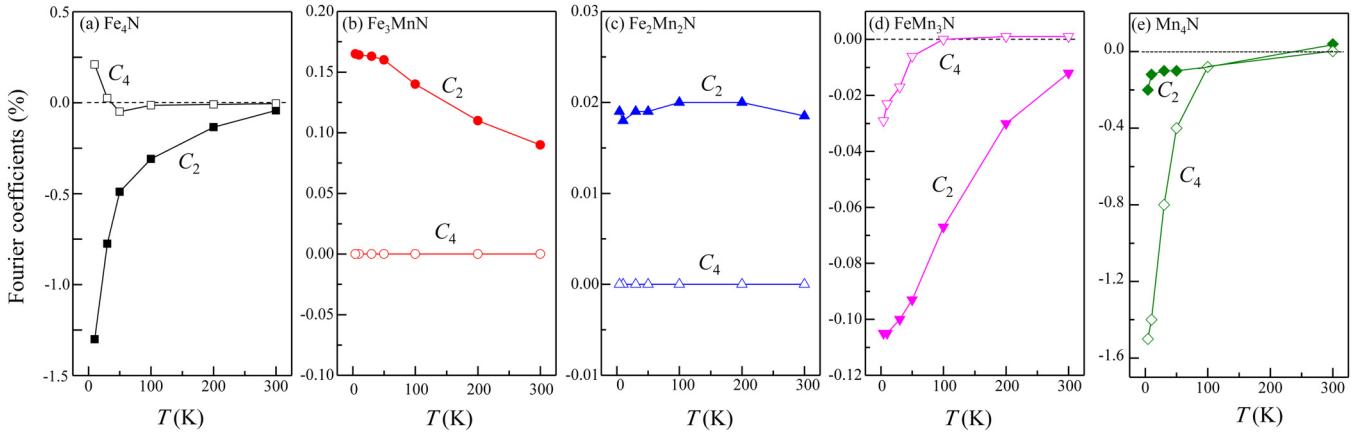

FIG. 7. Fourier coefficients C_2 and C_4 of the $[\rho(\phi)-\rho(90°)]/\rho(90°)$ curves of (a) Fe_4N, (b) Fe_3MnN, (c) Fe_2Mn_2N, (d) $FeMn_3N$, and (e) Mn_4N films measured in the temperature range 300–10 K.

where $H_{A(B)}$ is the exchange splitting of the sublattice A(B) and $D_{A(B),\xi(\gamma,\delta\varepsilon),\varsigma}$ is the partial D of the $d_\xi(d_\gamma, d_{\delta\varepsilon})$ orbital with ς-spin at E_F. The change in the sign of C_2 obtained for Mn_4N is explained by Eq. (11). The negative C_2 at low T means that $(D_{A,\gamma,\uparrow(\downarrow)}+D_{B,\gamma,\uparrow(\downarrow)})$ is smaller than $(D_{A,\delta\varepsilon,\uparrow(\downarrow)}+D_{B,\delta\varepsilon,\uparrow(\downarrow)})$. This magnitude correlation is reversed at high T like RT because of the shift of E_F, leading to the positive C_2. Because the P_σ is positive in Mn_4N, as shown in Table III and Refs. 51 and 52, the ↑-spin electrons dominate the electrical conduction and are scattered into ↑-spin d bands. As for the intermediate materials such as $FeMn_3N$, Fe_2Mn_2N, and Fe_3MnN, their electrical conduction is interpreted in the following way. In $FeMn_3N$, the ↑-spin electrons dominate the electrical conduction because of $P_\sigma > 0$ and are scattered into ↑-spin d bands just like in Mn_4N because of $D_\uparrow^{(d)} > D_\downarrow^{(d)}$. Here, $D_\uparrow^{(d)}[D_\downarrow^{(d)}]$ is the ↑-spin (↓-spin) D for 3d electrons at E_F. With increasing the Fe content further in Fe_2Mn_2N and Fe_3MnN, $D_\uparrow^{(d)}$ becomes smaller than $D_\downarrow^{(d)}$. Considering that the P_D is positive but the P_σ is negative in those materials, the ↓-spin electrons dominate the electrical conduction and are scattered into ↓-spin d bands. When the Fe content increases much further in Fe_4N, the ↓-spin electrons govern the electrical conduction due to $P_\sigma < 0$ and are scattered into ↓-spin d bands because of $D_\uparrow^{(d)} < D_\downarrow^{(d)}$. The above change in electrical conduction is likely caused by an increase in both exchange splitting and in E_F with increasing the Fe content.

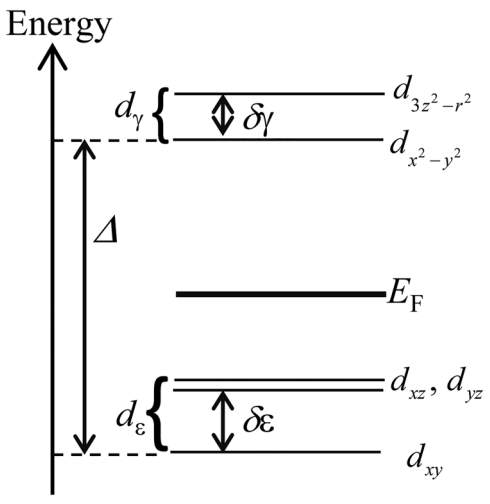

FIG. 8. Schematic energy levels of the 3d states in the tetragonal crystal field.[29]

Next, we consider the C_4 term. The dominant term in C_4 is proportional to the difference in the partial D at E_F among the d_ε states in Fig. 8.[29] The energy separation of the d_ε state into d_{xy}, d_{yz}, and d_{zx} states is caused by the tetragonal distortion. Therefore, the increase in $|C_4|$ with the decrease of T indicates the increase of the tetragonal distortion. The Fe_4N $|C_4|$ value only appears below 100 K as reported in Ref. 31. The Mn_4N $|C_4|$ value begins to increase around 100 K to reach a value of 1.5% at 10 K, which is more than seven times greater than the Mn_4N $|C_2|$ value. As reported in Refs. 13, 16, 18, 25, and 52, the in-plane tensile stress exists in the Mn_4N films, and therefore, the c/a value is smaller than 1 at RT, signifying tetragonal distortion in Mn_4N. A sharp increase of $|C_4|$ was also observed in $FeMn_3N$ ($c/a = 0.986$) (Ref. 25) in Fig. 7(d). In contrast, the C_4 value was almost 0 in Fe_3MnN and Fe_2Mn_2N over the whole T range in Figs. 7(b) and 7(c) even though the Fe_2Mn_2N film contained a higher tensile stress ($c/a = 0.985$) than that in the Mn_4N film ($c/a = 0.9991$) at RT.[25] It was reported that the lattice constant c of Fe_4N films decreased by 0.5% at 10 K compared to that at 300 K.[31] Thereby, it is still uncertain why such a small change in lattice constants causes a sharp increase of $|C_4|$ in Fe_4N. Thus, further theoretical and experimental investigations are mandatory to explain the T and ϕ dependences of C_2 and C_4 in more detail and especially to get the origin of C_4.

IV. CONCLUSION

We measured the AMR effect of 30 nm-thick $Fe_{4-x}Mn_xN$ ($x = 0$, 1, 2, 3, and 4) epitaxial films grown on MgO(001) substrates by MBE and investigated their magnetotransport properties at temperatures between 10 and 300 K. Experimentally measured saturation magnetizations were in agreement with those obtained by *ab initio* calculation. A positive AMR ratio was observed in Fe_3MnN and Fe_2Mn_2N

films, whereas Fe_4N, $FeMn_3N$, and Mn_4N films exhibited negative AMR ratios. The AMR ratio was negative in Fe_4N at $T \leq 300$ K, while the AMR ratio changed from positive to negative in Mn_4N at lower temperatures. Considering the sign of the spin polarization of the density of states at E_F calculated for $Fe_{4-x}Mn_xN$ ($x = 0$, 1, 2, 3, and 4), minority spin transport is dominant in Fe_4N, Fe_3MnN, and Fe_2Mn_2N, while majority spin transport is dominant in $FeMn_3N$ and Mn_4N. We also discussed the twofold and fourfold symmetries obtained in the AMR curves. The fourfold symmetry became pronounced at low temperatures in Fe_4N and $FeMn_3N$, and especially in Mn_4N. This effect was interpreted to originate from the tetragonal distortion; however, uncertainties remain about its origin. Thus, further investigations are mandatory especially to understand the origin of the fourfold symmetry in AMR curves.

ACKNOWLEDGMENTS

The magnetization measurements were performed with the help of Professor H. Yanagihara of the University of Tsukuba. The authors acknowledge Associate Professor K. Toko for his aid and encouragement to pursue this work. T.G. was financially supported by a Grant-in-Aid for Japan Society for the Promotion of Science Fellows (No. 16J02879).

[1]W. J. Takei, R. R. Heikes, and G. Shirane, Phys. Rev. **125**, 1893 (1962).
[2]F. Li, J. Yang, D. Xue, and R. Zhou, Appl. Phys. Lett. **66**, 2343 (1995).
[3]I. Pop, R. Muntean, and O. Pop, Mater. Lett. **28**, 155 (1996).
[4]S. Kokado, N. Fujima, K. Harigaya, H. Shimizu, and A. Sakuma, Phys. Rev. B **73**, 172410 (2006).
[5]M. S. Patwari and R. H. Victora, Phys. Rev. B **64**, 214417 (2006).
[6]K. Ito, G. H. Lee, H. Akinaga, and T. Suemasu, J. Cryst. Growth **322**, 63 (2011).
[7]Y. Takahashi, Y. Imai, and T. Kumagai, J. Magn. Magn. Mater. **323**, 2941 (2011).
[8]P. Monachesi, T. Björkman, T. Gasche, and O. Eriksson, Phys. Rev. B **88**, 054420 (2013).
[9]K. Ito, T. Sanai, Y. Yasutomi, S. Zhu, K. Toko, Y. Takeda, Y. Saitoh, A. Kimura, and T. Suemasu, J. Appl. Phys. **115**, 17C712 (2014).
[10]H. Sakakibara, H. Ando, Y. Kuroki, S. Kawai, K. Ueda, and H. Asano, J. Appl. Phys. **117**, 17D725 (2015).
[11]K. M. Ching, W. D. Chang, and T. S. Chin, J. Alloys Compd. **222**, 184 (1995).
[12]K. M. Ching, W. D. Chang, T. S. Chin, J. G. Duh, and H. C. Ku, J. Appl. Phys. **76**, 6582 (1994).
[13]Y. Yasutomi, K. Ito, T. Sanai, K. Toko, and T. Suemasu, J. Appl. Phys. **115**, 17A935 (2014).
[14]X. Shen, A. Chikamatsu, K. Shigematsu, Y. Hirose, T. Fukumura, and T. Hasegawa, Appl. Phys. Lett. **105**, 072410 (2014).
[15]M. Meng, S. X. Wu, L. Z. Ren, W. Q. Zhou, Y. J. Wang, G. L. Wang, and S. W. Li, Appl. Phys. Lett. **106**, 032407 (2015).
[16]K. Kabara and M. Tsunoda, J. Appl. Phys. **117**, 17B512 (2015).
[17]K. Kabara, M. Tsunoda, and S. Kokado, AIP Adv. **7**, 056416 (2017).
[18]K. Ito, Y. Yasutomi, K. Kabara, T. Gushi, S. Higashikozono, K. Toko, M. Tsunoda, and T. Suemasu, AIP Adv. **6**, 056201 (2016).
[19]T. Gushi, L. Vila, J. P. Attané, O. Fruchart, A. Marty, S. Pizzini, J. Vogel, F. Takata, A. Anzai, and T. Suemasu, in IEEE International Magnetics Conference CD-01, Singapore, 25 April 2018.
[20]M. Hayashi, L. Thomas, C. Rettner, R. Moriya, Y. B. Bazaliy, and S. P. Parkin, Phys. Rev. Lett. **98**, 037204 (2007).
[21]C. Paduani, J. Appl. Phys. **96**, 1 (2004).
[22]L. Chen, J. Appl. Phys. **100**, 113717 (2006).
[23]H. Wu, H. Sun, and C. Chen, Phys. Rev. B **91**, 064102 (2015).
[24]J. Martínez, L. Lopardo, and J. Desimoni, J. Alloys Compd. **557**, 218 (2013).
[25]A. Anzai, F. Takata, T. Gushi, K. Toko, and T. Suemasu, J. Cryst. Growth **489**, 20 (2018).
[26]S. Kokado, N. Fujima, K. Harigaya, H. Shimizu, and A. Sakuma, Phys. Rev. B **73**, 172410 (2006).
[27]S. Kokado, M. Tsunoda, K. Harigaya, and A. Sakuma, J. Phys. Soc. Jpn. **81**, 024705 (2012).
[28]S. Kokado and M. Tsunoda, Adv. Mater. Res. **750**, 978 (2013).
[29]S. Kokado and M. Tsunoda, J. Phys. Soc. Jpn. **84**, 094710 (2015).
[30]M. Tsunoda, Y. Komasaki, S. Kokado, S. Isogami, C.-C. Chen, and M. Takahashi, Appl. Phys. Express **2**, 083001 (2009).
[31]M. Tsunoda, H. Takahashi, S. Kokado, Y. Komasaki, A. Sakuma, and M. Takahashi, Appl. Phys. Express **3**, 113003 (2010).
[32]K. Ito, K. Kabara, H. Takahashi, T. Sanai, K. Toko, T. Suemasu, and M. Tsunoda, Jpn. J. Appl. Phys. **51**, 068001 (2012).
[33]K. Kabara, M. Tsunoda, and S. Kokado, Appl. Phys. Express **7**, 063003 (2014).
[34]K. Ito, K. Kabara, T. Sanai, K. Toko, Y. Imai, M. Tsunoda, and T. Suemasu, J. Appl. Phys. **116**, 053912 (2014).
[35]Z. R. Li, X. P. Feng, X. C. Wang, and W. B. Mi, Mater. Res. Bull. **65**, 175 (2015).
[36]F. J. Yang, Y. Sakuraba, S. Kokado, Y. Kota, A. Sakuma, and K. Takanashi, Phys. Rev. B **86**, 020409(R) (2012).
[37]Y. Sakuraba, S. Kokado, Y. Hirayama, T. Furubayashi, H. Sukegawa, S. Li, Y. K. Takahashi, and K. Hono, Appl. Phys. Lett. **104**, 172407 (2014).
[38]K. Srinivas, M. Mannivel Raja, S. Arumugam, and S. V. Kamat, Physica B **448**, 167 (2014).
[39]Y. Du, G. Z. Xu, E. K. Liu, G. J. Li, H. G. Zhang, S. Y. Yu, W. H. Wang, and G. H. Wu, J. Magn. Magn. Mater. **335**, 101 (2013).
[40]K. Kabara, M. Tsunoda, and S. Kokado, AIP Adv. **6**, 055818 (2016).
[41]X. Li, H. Li, M. Jamali, and J. P. Wang, AIP Adv. **7**, 125303 (2017).
[42]F. Takata, K. Kabara, K. Ito, M. Tsunoda, and T. Suemasu, J. Appl. Phys. **121**, 023903 (2017).
[43]G. Kresse and J. Furthmüller, Comput. Mater. Sci. **6**, 15 (1996).
[44]P. E. Blöchl, Phys. Rev. B **50**, 17953 (1994).
[45]J. P. Perdew, K. Burke, and M. Ernzerhof, Phys. Rev. Lett. **77**, 3865 (1996).
[46]G. Henkelman, A. Arnaldsson, and H. Jonsson, Comput. Mater. Sci. **36**, 354 (2006).
[47]R. C. Reynolds, Jr., Clays Clay Miner. **34**, 359 (1986).
[48]A. Fert and I. A. Campbell, Phys. Rev. Lett. **21**, 1190 (1968).
[49]I. A. Campbell, A. Fert, and O. Jaoul, J. Phys. C **3**, S95 (1970).
[50]W. Döring, Ann. Phys. **424**, 259 (1938).
[51]Y. Imai, Y. Takahashi, and T. Kumagai, J. Magn. Magn. Mater. **322**, 2665 (2010).
[52]M. Tsunoda and K. Kabara, in International Conference of the Asian Union of Magnetics Societies (ICAUMS) 2pPS-47, Nara, 2 October 2012.